

# Constraints on the evolution of the relationship between HI mass and halo mass in the last 12 Gyr

Hamsa Padmanabhan<sup>1\*</sup> and Girish Kulkarni<sup>2†</sup>

<sup>1</sup> *Institute for Astronomy, ETH Zurich, Wolfgang-Pauli-Strasse 27, CH-8093 Zürich, Switzerland*

<sup>2</sup> *Institute of Astronomy and Kavli Institute for Cosmology, University of Cambridge, Madingley Road, Cambridge CB3 0HA, UK*

Accepted —. Received —; in original form —

## ABSTRACT

The neutral hydrogen (HI) content of dark matter haloes forms an intermediate state in the baryon cycle that connects the hot shock-heated gas and cold star-forming gas in haloes. Measurement of the relationship between HI mass and halo mass therefore puts important constraints on galaxy formation models. We combine radio observations of HI in emission at low redshift ( $z \sim 0$ ) with optical/UV observations of HI in absorption at high redshift ( $1 < z < 4$ ) to derive constraints on the evolution of the HI-mass halo-mass (HIHM) relation from redshift  $z = 4$  to  $z = 0$ . We find that one can model the HIHM relation similar to the stellar-mass halo-mass (SHM) relation at  $z \sim 0$ . At  $z = 0$ , haloes with mass  $10^{11.7} M_{\odot}$  have the highest HI mass fraction ( $\sim 1\%$ ), which is about four times smaller than their stellar mass fraction. We model the evolution of the HIHM relation in a manner similar to that of the SHM relation. Combining this parameterisation with a redshift- and mass-dependent modified Navarro-Frenk-White (NFW) profile for the HI density within a halo, we draw constraints on the evolution of the HIHM relation from the observed HI column density, incidence rate, and clustering bias at high redshift. We compare these findings with results from hydrodynamical simulations and other approaches in the literature, and find the models to be consistent with each other at the 68% confidence level.

**Key words:** cosmology: observations – galaxies: evolution – radio lines: galaxies

## 1 INTRODUCTION

Understanding the evolution of neutral hydrogen (HI) in dark matter haloes is important for models of galaxy formation (Somerville & Davé 2015; Blanton & Moustakas 2009; Barkana 2016). The HI content of dark matter haloes forms an intermediate state in the baryon cycle that connects the hot shock-heated gas and star-forming molecular gas in haloes (Bouché et al. 2010; Fu et al. 2010; Krumholz & Dekel 2012). Constraints on HI in galaxies therefore reveal the role of gas dynamics, cooling, and regulatory processes such as stellar feedback and gas inflow and outflow in galaxy formation (Prochaska & Wolfe 2009; van de Voort et al. 2011; Bird et al. 2015; Kauffmann et al. 2015; Bahé et al. 2016). HI also traces environmental processes like satellite quenching, tidal interactions and ram-pressure stripping (Fabello et al. 2012; Li et al. 2012; Zhang et al. 2013; Lagos et al. 2014). The average HI mass content of dark matter haloes can be expressed as an HI-mass halo-mass (HIHM) relation.

At low redshifts ( $z \sim 0$ ), constraints on HI in galax-

ies are derived from the observations of the 21 cm emission line of hydrogen in large-area blind galaxy surveys like the HI Parkes All Sky Survey (HIPASS, Meyer et al. 2004) and the Arecibo Fast Legacy ALFA survey (ALFALFA, Giovanelli et al. 2005), which provide measurements of the mass function and clustering of HI-selected galaxies. There are also targeted surveys such as The HI Nearby Galaxy Survey (THINGS, Walter et al. 2008), the Galex Arecibo SDSS Survey (GASS, Catinella et al. 2010), and the Westerbork HI survey of Spiral and Irregular Galaxies (WHISP, van der Hulst et al. 2001), which focus on a smaller number of resolved galaxies. Efforts are also currently underway to constrain the density and clustering of HI using intensity mapping without resolving individual galaxies (Chang et al. 2010; Masui et al. 2013; Switzer et al. 2013). In the future, current and upcoming facilities such as MeerKAT (Jonas 2009), the Square Kilometre Array (SKA, Santos et al. 2015) and its pathfinders, and the Canadian Hydrogen Intensity Mapping Experiment (CHIME, Bandura et al. 2014), will provide unprecedented insight into the evolution of the cosmic neutral hydrogen content across redshifts.

Unfortunately, the intrinsic faintness of the 21 cm line and the limits of current radio facilities hamper direct detec-

\* Email: hamsa.padmanabhan@phys.ethz.ch

† Email: kulkarni@ast.cam.ac.uk

tion of HI from individual galaxies at redshifts above  $z \sim 0.1$ . Spectral stacking has been used to probe the HI content of undetected sources out to redshifts  $z \sim 0.24$  (Lah et al. 2007, 2009; Rhee et al. 2013; Delhaize et al. 2013). At higher redshifts, therefore, constraints on the distribution and evolution of HI in galaxies come chiefly from high column density Lyman- $\alpha$  absorption systems (Damped Lyman- $\alpha$  Absorbers; DLAs) with column density  $N_{\text{HI}} > 10^{20.2} \text{ cm}^{-2}$  in the spectra of bright background sources such as quasars. DLAs are the main reservoir of HI between redshifts  $z \sim 2-5$ , containing  $> 80\%$  of the cosmic HI content (Wolfe et al. 1986; Lanzetta et al. 1991; Gardner et al. 1997; Prochaska & Wolfe 2009; Rao et al. 2006; Noterdaeme et al. 2012; Zafar et al. 2013). At low redshift, DLAs have been found to be associated with galaxies (Lanzetta et al. 1991) and to contain the vast majority ( $\sim 81\%$ ) of the HI gas in the local universe (Zwaan et al. 2005b). At high redshift, the kinematics of DLAs may support the hypothesis that they probe HI in large rotating disks (Prochaska & Wolfe 1997; Maller et al. 2001; Bird et al. 2015) or proto-galactic clumps (Haehnelt et al. 1998). The three-dimensional clustering of DLAs (Font-Ribera et al. 2012) points to DLAs being preferentially hosted by dark matter haloes with mass  $M \sim 10^{11} M_{\odot}$  at redshift  $z \sim 3$ .

Semi-analytical models and hydrodynamical simulations have provided clues towards the evolution of HI in galaxies and its relation to star-formation, feedback and galaxy evolution (Davé et al. 2013; Duffy et al. 2012; Lagos et al. 2011; Obreschkow et al. 2009; Nagamine et al. 2007; Pontzen et al. 2008; Tescari et al. 2009; Hong et al. 2010; Cen 2012; Fu et al. 2012; Kim et al. 2013; Bird et al. 2014; Popping et al. 2009, 2014; Crain et al. 2016; Kim et al. 2016; Martindale et al. 2016). Semi-analytical methods (e.g., Berry et al. 2014; Popping et al. 2014; Somerville et al. 2015) typically reproduce the HI mass functions and the HI-to-stellar-mass scaling relations found in low-redshift HI observations and DLA observables. Simulation techniques have also been used to model DLA populations at higher redshifts (Pontzen et al. 2008) and their relation to galaxy formation and feedback processes (Bird et al. 2014; Rahmati et al. 2013; Rahmati & Schaye 2014). Hydrodynamical simulations suggest that DLAs are hosted in haloes with mass  $10^{10}-10^{11} h^{-1} M_{\odot}$  (e.g., Bird et al. 2014). In the presence of strong stellar feedback, these simulations can reproduce the observed abundance and clustering of DLAs but end up having an excess of HI at low redshifts ( $z < 3$ ).

Analytical techniques offer complementary insight into the processes governing the HI content of dark matter halos. Analytical methods have been used for modelling 21 cm intensity mapping observables, particularly the HI bias and power spectrum (Marín et al. 2010; Wyithe & Brown 2010; Sarkar et al. 2016) as well as DLAs (Haehnelt et al. 1996, 1998; Barnes & Haehnelt 2009, 2010; Kulkarni et al. 2013; Barnes & Haehnelt 2014). These models use prescriptions for assigning HI mass to dark matter halos as inputs to the model, either directly or in conjunction with cosmological simulations (Bagla et al. 2010; Marín et al. 2010; Gong et al. 2011; Guha Sarkar et al. 2012). In Padmanabhan et al. (2016), the 21-cm- and DLA-based analytical approaches are combined towards a consistent model of HI evolution across redshifts. It is found that a model that is consistent with low-redshift radio as well as high-redshift optical/UV obser-

vations requires a fairly rapid transition of HI from low-mass to higher-mass haloes at high redshifts. A more complete statistical data-driven approach (Padmanabhan & Refregier 2016) constrains the HIHM relation using low- and high-redshift observations in a halo model framework.

An essential ingredient in analytical techniques is therefore the HIHM relation. In this paper, we employ the technique of abundance matching to quantify the observational constraints on the HIHM relation in the post-reionization Universe. Abundance matching has been widely used to describe the relation between the stellar mass of galaxies and the mass of their host dark matter halos (Vale & Ostriker 2004, 2006; Conroy et al. 2006; Behroozi et al. 2010; Guo et al. 2010; Shankar et al. 2006a; Moster et al. 2010, 2013). The basic assumption involved is that there is a monotonic relationship between a galaxy property (say, stellar mass or galaxy luminosity) and the host dark matter halo property (say, the host halo mass). In its simplest form, abundance matching involves matching the cumulative abundance of galaxies to that of their (sub)haloes, thereby assigning the most luminous galaxies to the most massive haloes. The mapping between the underlying galaxy property and the host halo mass can be derived from this. A key feature of this approach is that being completely empirical<sup>1</sup>, it is free from the uncertainties involved in physical models of HI and galaxy evolution. It is therefore a complementary analysis to forward modelling techniques, including semi-analytical models and hydrodynamical simulations.

The HI mass function (Rao & Briggs 1993) is the radio equivalent of the optical luminosity function in galaxies and is an important statistical quantity in the observations of gas-rich galaxies. It measures the volume density of HI-selected galaxies as a function of the HI mass and simulations suggest that its shape is a more sensitive probe of some aspects of galaxy formation physics than the galaxy luminosity function (Kim et al. 2013). At low redshifts, the HI mass function is fairly well-constrained over four decades in HI mass (Zwaan et al. 2005a; Martin et al. 2010). Papastergis et al. (2013) constrained the HIHM relation at low redshift using ALFALFA data and found that the observed clustering of HI was reproduced well by this approach. In this work, we describe the results of abundance matching HI mass to dark matter halo mass using the low-redshift radio observations of the HI mass function (Zwaan et al. 2005a; Martin et al. 2010) and then evolve the relation using the complementary information available through DLA measurements at high redshift. The combination of the radio data at low redshifts and DLA observations at higher redshifts constrains a multi-epoch HI-halo mass relation with the available data. We also compare how the results from this approach are consistent with those from studies in previous literature.

The paper is organized as follows. In Section 2, we detail the abundance matching technique and apply it to three low-redshift HI mass function measurements. We also combine the resultant HIHM relation with the stellar-mass halo-mass (SHM) relation to discuss the HI-to-stellar-mass ratio in low-redshift galaxies. In Section 3, we extend the low-

<sup>1</sup> A caveat is that the halo mass function being used is theoretical, and the assumption of matching the most massive haloes is involved.

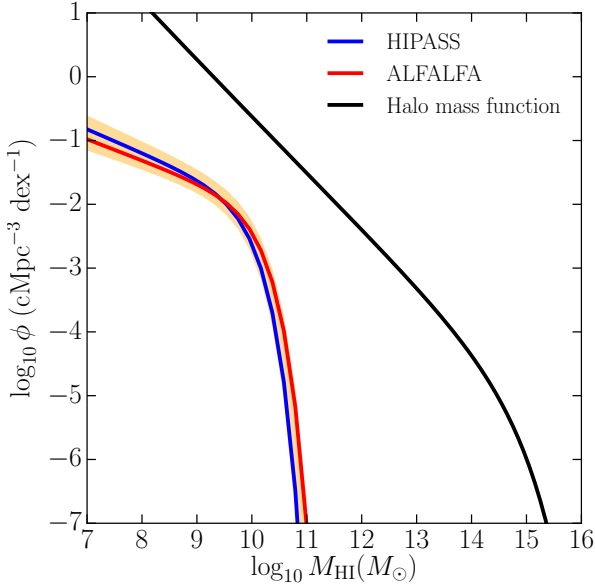


**Figure 1.** The blue and red curves show the HI mass functions derived from the HIPASS (Zwaan et al. 2005a) and ALFALFA data (Martin et al. 2010), respectively. The shaded region shows the combined uncertainty. The black curve shows the halo mass function.

redshift HIHM relation to higher redshifts using measurements of DLA column density distribution and clustering. We compare the relation so derived with other HI models in the literature, and conclude in Section 4.

## 2 HIHM RELATION AT LOW REDSHIFT

We derive the HIHM relation at  $z \sim 0$  by abundance matching dark matter haloes with HI-selected galaxies. We use the HI mass function from the HIPASS (Meyer et al. 2004) and ALFALFA (Martin et al. 2010) datasets, the latter derived using the  $1/V_{\max}$  as well as the 2DSWML (2-Dimensional StepWise Maximum Likelihood) methods:

- HIPASS: This complete catalogue of HI sources contains 4,315 galaxies (Meyer et al. 2004). The HI mass function  $\phi(M_{\text{HI}})$  is fitted by a Schechter function using the 2-Dimensional StepWise Maximum Likelihood (2DSWML) method, with a total of 4010 galaxies. The effective volume  $V_{\text{eff}}$  is calculated for each galaxy individually and the values of  $1/V_{\text{eff}}$  are summed in bins of HI mass to obtain the 2DSWML mass function. The resultant best-fit parameters are  $\alpha = -1.37 \pm 0.03 \pm 0.05$ ,  $\log(M_*/M_{\odot}) = 9.80 \pm 0.03 \pm 0.03h_{75}^{-2}$  and  $\phi^* = (6.0 \pm 0.8 \pm 0.6) \times 10^{-3}h_{75}^3 \text{ Mpc}^{-3}$  (the two error values show statistical and systematic errors, respectively; Zwaan et al. 2005a). The distribution of HI masses is calculated using 30 equal-sized mass bins spanning  $6.4 < \log_{10} M_{\text{HI}} < 10.8$  (in  $M_{\odot}$ ).

- ALFALFA: This catalogue contains 10,119 sources to form the largest available sample of HI-selected galaxies (Martin et al. 2010). The ALFALFA survey measures the HI mass function by using both the 2DSWML as well as

the  $1/V_{\max}$  methods. The HI mass function is fitted with the Schechter form, with the best-fitting parameters  $\phi^* = (4.8 \pm 0.3) \times 10^{-3}h_{70}^3 \text{ Mpc}^{-3}$ ,  $\log(M_*/M_{\odot}) + 2\log(h_{70}) = 9.95 \pm 0.04$ , and  $\alpha = -1.33 \pm 0.03$  with the  $1/V_{\max}$  method, and  $\phi^* = (4.8 \pm 0.3) \times 10^{-3}h_{70}^3 \text{ Mpc}^{-3}$ ,  $\log(M_*/M_{\odot}) + 2\log(h_{70}) = 9.96 \pm 0.2$ , and  $\alpha = -1.33 \pm 0.02$  with the 2DSWML method. The two determinations of the HI mass function are in good agreement.<sup>2</sup>

To match HI-selected galaxies to dark matter haloes, we use the Sheth-Tormen (Sheth & Tormen 2002) form of the dark matter halo mass function. Figure 1 shows the comparison of the three HI mass functions mentioned above with the halo mass function, which is shown by the solid black curve. This corresponds to the assumption that each dark matter halo hosts one HI galaxy with its HI mass proportional to the host dark matter halo mass. The shaded region in Figure 1 shows the combined uncertainty in the observed HI mass functions. Matching the abundance of the halo mass function and the fitted HI mass function then leads to the relation between the HI mass and the halo mass (e.g., Vale & Ostriker 2004):

$$\int_{M(M_{\text{HI}})}^{\infty} \frac{dn}{d\log_{10} M'} d\log_{10} M' = \int_{M_{\text{HI}}}^{\infty} \phi(M'_{\text{HI}}) d\log_{10} M'_{\text{HI}} \quad (1)$$

where  $dn/d\log_{10} M$  is the number density of dark matter haloes with logarithmic masses between  $\log_{10} M$  and  $\log_{10}(M + dM)$ , and  $\phi(M_{\text{HI}})$  is the corresponding number density of HI galaxies in logarithmic mass bins. Solving Equation (1) gives a relation between the HI-mass  $M_{\text{HI}}$  and the halo mass  $M$ . Note that this approach assumes that there is a monotonic relationship between  $M_{\text{HI}}$  and  $M$ .

Solving Equation (1) in the mass range  $10^6 M_{\odot} < M_{\text{HI}} < 10^{11} M_{\odot}$ , we show the resultant HIHM relation in the top panel of Figure 2. The red curve shows the HIHM relation obtained from the ALFALFA data, while the blue curve shows the same for the HIPASS data. We find that the HI mass monotonically increases as a function of the halo mass and changes slope at a characteristic value of the halo mass. This behaviour is qualitatively similar to the SHM relation (Moster et al. 2013), which is shown by the dashed red curve in the top panel of Figure 2. For small mass haloes, the HI mass is nearly equal to the stellar mass. But the HI mass decreases more rapidly than the stellar mass as a function of halo mass, and for high mass haloes the HI mass is down to almost a tenth of the stellar mass. The characteristic mass for the HIHM relation is also slightly smaller ( $10^{11.7} M_{\odot}$ ) than that for the SHM relation ( $\sim 10^{12} M_{\odot}$ ). The HIHM relation is shown as the ratio of the HI and halo masses in the lower panel of Figure 2. The peak HI mass fraction is about 1%, and this reduces down to 0.01% at both high and low masses. The peak HI mass fraction is in good agreement with the abundance matching estimates of Rodríguez-Puebla et al. (2011); Evoli et al. (2011); Baldry et al. (2008) and the direct estimate of Papastergis et al. (2012) for the baryonic mass fraction. It had been found that the clustering of the HI selected galaxies in ALFALFA

<sup>2</sup> In the figures, we only indicate the ALFALFA 2DSWML mass function fit for clarity.

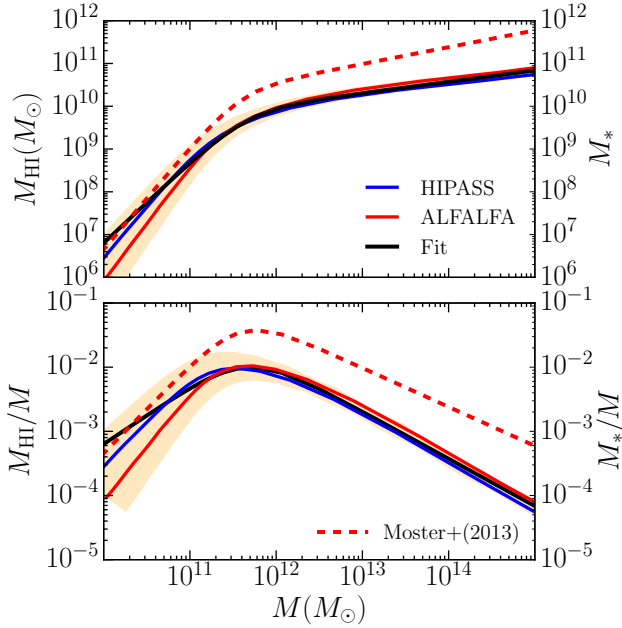


**Figure 2.** *Top panel:* The HIHM relation at  $z = 0$  derived from HIPASS (blue curve) and ALFALFA (red curve) HI mass functions. The black curve shows a combined fit to the mass functions using the parametric form of Equation (2). The shaded region shows the error in the fit. *Lower panel:* The HI mass fraction,  $M_{\text{HI}}/M$  as a function of halo mass  $M$  at  $z = 0$ . Also shown for comparison in both panels is the SHM relation (Moster et al. 2013).

(Papastergis et al. 2013) was also well-matched by abundance matching at  $z \sim 0$ , and the cold gas fraction showed a maximum at halo masses close to  $10^{11.1-11.3} M_{\odot}$ , which was lower than the corresponding peak for the stellar mass fraction ( $10^{11.8} M_{\odot}$ ).

We parameterise the HIHM relation by a function of the form introduced for the SHM relation by Moster et al. (2013),

$$M_{\text{HI}} = 2N_{10}M \left[ \left( \frac{M}{M_{10}} \right)^{-b_{10}} + \left( \frac{M}{M_{10}} \right)^{y_{10}} \right]^{-1}. \quad (2)$$

We fit the HIHM relation by the function of this form using non-linear least squares. The best-fitting values of the free parameters are  $M_{10} = (4.58 \pm 0.19) \times 10^{11} M_{\odot}$ ,  $N_{10} = (9.89 \pm 4.89) \times 10^{-3}$ ,  $b_{10} = 0.90 \pm 0.39$  and  $y_{10} = 0.74 \pm 0.03$ . The errors here are estimated by propagating the uncertainties in Figure 1. The best-fit HIHM relations are shown in Figure 2 (black curves), with the corresponding error indicated by the shaded region.

## 2.1 The HI-mass stellar-mass relation

We can combine our derived HIHM relation with known SHM relations to understand the relationship between the HI mass and stellar mass in dark matter haloes. Moster et al. (2013) use a multi-epoch abundance matching method with observed stellar mass functions (SMFs) to describe the evolution of the SHM relation across redshifts. At each redshift, they parameterise the SHM relation using the functional

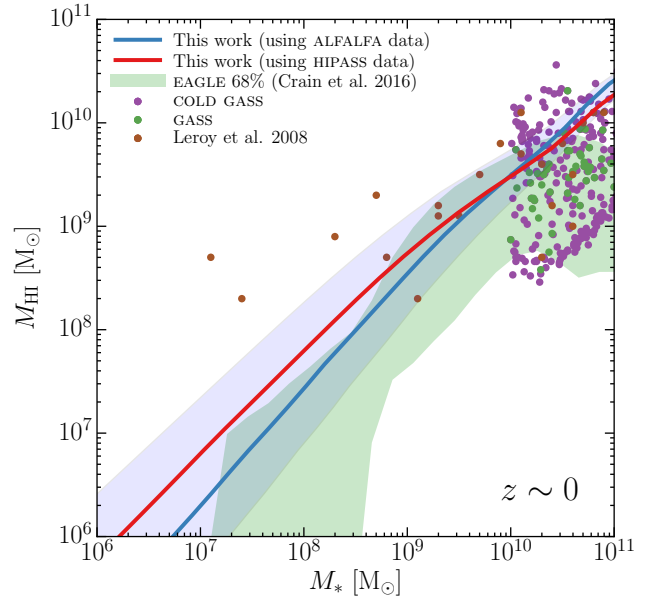


**Figure 3.** The HI-mass stellar-mass relation obtained by abundance matching combined with the SHM relation determined by Moster et al. (2013), are shown by the solid curves. The 68% scatter in the relation is indicated by the blue band. The green band shows the region around the median in which 68% of the galaxies in the EAGLE reference simulation lie on this plane (Crain et al. 2016). Also shown are the data from individual objects detected in the GASS and COLD GASS surveys, and the nearby galaxies in HERACLES and THINGS (Leroy et al. 2008).

form in Equation (2). At low redshifts, the SMFs of Li & White (2009) based on the Sloan Digital Sky Survey (SDSS) DR7 (York et al. 2000; Abazajian et al. 2009) are used, along with the observations of Baldry et al. (2008). At higher redshifts, the SMFs by Pérez-González et al. (2008) are used for massive galaxies, and those by Santini et al. (2012) for the low mass galaxies. From the results of abundance matching, the mean SHM relation is obtained, which is then used to populate haloes in the Millennium (MS-I; Springel et al. 2005) and the Millennium - II (MS-II; Boylan-Kolchin et al. 2009) simulations with galaxies. From this, the model stellar mass functions are derived and directly compared to observations to constrain the free parameters in the SHM relation. The resulting mean stellar mass fraction at  $z \sim 0$  is shown by the dashed line in Figure 2.

We use the Moster et al. (2013) results for the SHM relation, coupled to our abundance matching results for HIHM to arrive at a HI-mass stellar-mass relation. This is shown by the solid red and blue curves in Figure 3 for HIPASS and ALFALFA respectively. The 68% scatter in the relation is indicated by the blue band. For comparison, we also show the measurements from 750 galaxies in the redshift range  $0.025 < z < 0.05$  and  $M_* > 10^{10} M_{\odot}$  from the GALEX Arecibo SDSS survey (GASS; Catinella et al. 2010, 2013), and 366 galaxies from the COLD GASS survey (Saintonge et al. 2011a,b; Catinella et al. 2012). We also show results from Leroy et al. (2008), which is a compilation of individual galaxies detected in the HERA CO Line Extragalactic Survey (HERACLES; Leroy et al. 2009) that are part of The HI Nearby Galaxy Survey (THINGS; Walter et al. 2008), which

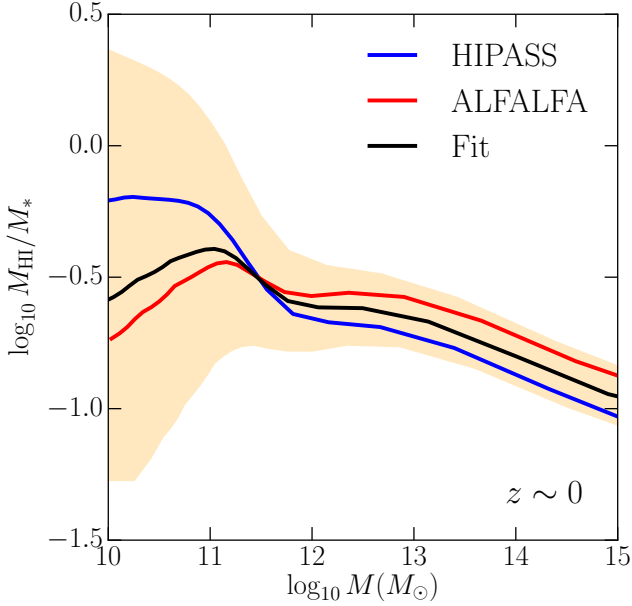


**Figure 4.** The HI-mass to stellar-mass ratio as a function of the halo mass at  $z \sim 0$ . The blue and red curves combine our results for HIPASS and ALFALFA data, respectively, with the SHM relation from [Moster et al. \(2013\)](#). The parametrized fit is indicated by the black curve. The shaded region shows the uncertainty in the HI-mass to stellar-mass ratio obtained by propagating errors from Figure 2.

covers HI masses in the range  $(0.01\text{--}14) \times 10^9 M_\odot$ . These measurements are consistent with our result, although the observational data exhibit a somewhat large scatter. We note that the HI-stellar mass relation from the ALFALFA data and the THINGS data show some discrepancy at low stellar masses (also seen in [Popping et al. \(2015\)](#), which matches the data in [Leroy et al. \(2008\)](#), but has difficulty matching the ALFALFA data mass function at low HI masses). However, the main aim of the present work is to provide an understanding of the HI-mass halo-mass relation, and as such, we do not conjecture on the observed discrepancy of the [Leroy et al. \(2008\)](#) results with the ALFALFA data. We also compare our HI-mass stellar-mass relation with that found in the EAGLE hydrodynamical simulations ([Schaye et al. 2015](#); [Crain et al. 2015](#)). The EAGLE simulations model the formation and evolution of galaxies in the presence of various feedback processes. They also model the HI content of galaxies by using calibrated fitting functions from radiative transfer simulations to estimate self-shielding, and also employing empirical relations to correct for molecular gas formation ([Crain et al. 2016](#)). The green band in Figure 3 shows the region around the median on the HI-mass stellar-mass diagram occupied by 68% of galaxies in the reference EAGLE simulation (labelled “L100N1504” in [Schaye et al. 2015](#)). Our results are in good agreement with the EAGLE predictions, except possibly at the highest stellar masses ( $M_* > 10^{10} M_\odot$ ) where the HI mass in EAGLE galaxies starts to decrease. This is likely a reflection of the AGN feedback in EAGLE, that heats and expunges cold gas from high mass galaxies by their massive central black holes ([Crain et al. 2016](#)).

$z$	Observable	Source
$\sim 1$	$\Omega_{\text{HI}} b_{\text{HI}}$	<a href="#">Switzer et al. (2013)</a>
	$f_{\text{HI}}$	<a href="#">Rao et al. (2006)</a>
	$dN/dX$	<a href="#">Rao et al. (2006)</a>
2.3	$\Omega_{\text{DLA}}$	<a href="#">Zafar et al. (2013)</a>
	$f_{\text{HI}}$	<a href="#">Noterdaeme et al. (2012)</a>
	$b_{\text{DLA}}$	<a href="#">Font-Ribera et al. (2012)</a>
	$dN/dX$	<a href="#">Zafar et al. (2013)</a>
$> 3$	$dN/dX$	<a href="#">Zafar et al. (2013)</a>

**Table 1.** High-redshift data used in this paper. The measurement of  $\Omega_{\text{HI}} b_{\text{HI}}$  comes from HI intensity mapping at  $z \sim 0.8$  by [Switzer et al. \(2013\)](#). [Rao et al. \(2006\)](#) use measurements of absorption systems at median redshifts  $z \sim 0.609$  and  $z \sim 1.219$  to derive the DLA parameters. All other data come from Lyman- $\alpha$  absorption measurements using high-redshift quasar spectra.

Figure 4 shows the HI-mass to stellar-mass ratio as a function of the halo mass. The blue and red curves show the results for HIPASS and ALFALFA respectively, and the black curve shows the parametrized fit. In each case, we obtain the HI-mass to stellar-mass ratio by combining our HIHM relation with the SHM relation of [Moster et al. \(2013\)](#). The HI-mass to stellar-mass ratio is about 25% in a rather broad range of halo masses from  $10^{11}$  to  $10^{13} M_\odot$ . The ratio decreases to about 10% at halo masses above this range, and is more uncertain below this range, due to the uncertainty in the data and the fitting (Fig. 2 lower panel) at lower masses. The shaded regions show the uncertainty in the HI-mass to stellar-mass ratio, obtained by propagating the errors from Figure 2.

### 3 HIHM RELATION AT HIGH REDSHIFT

Due to the intrinsic faintness of the 21 cm line, the direct detection of HI from resolved galaxies is difficult at redshifts above  $z \sim 0.1$ . At higher redshifts ( $z < 5$ ), therefore, constraints on the distribution and evolution of HI in galaxies mainly come from high column density Lyman- $\alpha$  absorption systems (Damped Lyman- $\alpha$  Absorbers; DLAs) with column densities  $N_{\text{HI}} > 10^{20.3} \text{ cm}^{-2}$  in the spectra of bright background sources such as quasars. The relevant observables at these redshifts are the incidence rate  $dN/dX$  of DLAs, the column density distribution  $f_{\text{HI}}(N_{\text{HI}}, z)$  of DLAs at high column densities, the three-dimensional clustering of DLAs as quantified by their clustering bias relative to the underlying dark matter, and the total amount of neutral hydrogen in DLAs ([Wolfe et al. 1986](#); [Lanzetta et al. 1991](#); [Gardner et al. 1997](#); [Prochaska & Wolfe 2009](#); [Rao et al. 2006](#); [Noterdaeme et al. 2012](#); [Zafar et al. 2013](#)). A detailed summary of the low- and high-redshift HI observables is provided in [Padmanabhan et al. \(2015\)](#). We now extend the HIHM relation obtained at  $z = 0$  to higher redshifts by using these observables. Throughout the analysis, we use the cosmological parameters  $h = 0.71$ ,  $\Omega_m = 0.281$ ,  $\Omega_\Lambda = 0.719$ ,  $\sigma_8 = 0.8$ ,  $n_s = 0.964$ .

#### 3.1 Modelling the HI observables

To model the distribution of HI density within individual dark matter haloes, we use the redshift- and mass-dependent

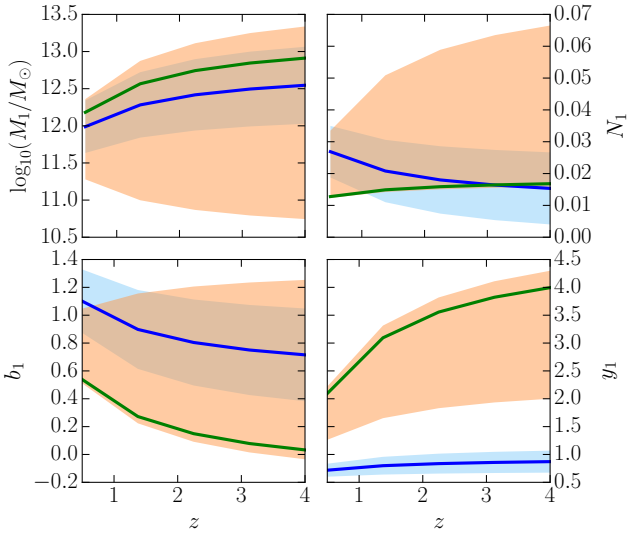


**Figure 5.** The evolution of the parameters of the HIHM relation (Equation 14). The green curves show our best-fit parameter inferences with 68% confidence intervals shown by the orange shaded region. For comparison, the evolution of the corresponding quantities for the SHM relation of Moster et al. (2013) is shown in blue.

modified Navarro-Frenk-White (NFW; Navarro et al. 1996) profile introduced by Barnes & Haehnelt (2014):

$$\rho_{\text{HI}}(r) = \frac{\rho_0 r_s^3}{(r + 0.75r_s)(r + r_s)^2}, \quad (3)$$

where  $r_s$  is the scale radius defined as  $r_s = R_v(M)/c(M, z)$ , with  $R_v(M)$  being the virial radius of the halo. The halo concentration parameter,  $c(M, z)$  is approximated by:

$$c(M, z) = c_{\text{HI}} \left( \frac{M}{10^{11} M_\odot} \right)^{-0.109} \left( \frac{4}{1+z} \right). \quad (4)$$

The profile in Equation (3) is motivated by the analytical modelling of cooling in multiphase halo gas by Maller & Bullock (2004). In the above equation,  $c_{\text{HI}}$  is a free parameter, the concentration parameter for the HI, analogous to the dark matter halo concentration  $c_0 = 3.4$  (Macciò et al. 2007). The value of this parameter can be constrained by fitting to the observations. The  $\rho_0$  in Equation (3) is determined by normalization to the total HI mass:

$$\int_0^{R_v(M)} 4\pi r^2 \rho_{\text{HI}}(r) dr = M_{\text{HI}}(M) \quad (5)$$

Thus, both the HI-halo mass relation as well as the radial distribution of HI are required for constraining the HI profile.

The DLA based quantities at different redshifts can now be computed by defining the column density of a halo at impact parameter  $s$  as (Barnes & Haehnelt 2014; Padmanabhan et al. 2016):

$$N_{\text{HI}}(s) = \frac{2}{m_H} \int_0^{\sqrt{R_v(M)^2 - s^2}} dl \rho_{\text{HI}}(\sqrt{s^2 + l^2}) \quad (6)$$

where  $m_H$  is the hydrogen atom mass and  $R_v(M)$  is the virial radius associated with a dark matter halo of mass  $M$ . We define the DLA cross-section of the halo as  $\sigma_{\text{DLA}} = \pi s_*^2$ ,

where  $s_*$  is defined such that  $N_{\text{HI}}(s_*) = 10^{20.3} \text{ cm}^{-2}$ . The clustering bias of DLAs,  $b_{\text{DLA}}$ , can then be written as

$$b_{\text{DLA}}(z) = \frac{\int_0^\infty dM n(M, z) b(M, z) \sigma_{\text{DLA}}(M, z)}{\int_0^\infty dM n(M, z) \sigma_{\text{DLA}}(M, z)}, \quad (7)$$

where  $n(M, z)$  is the comoving halo mass function and  $b(M, z)$  is the clustering bias factor of haloes Scoccimarro et al. (2001). The DLA incidence  $dN/dX$  can be calculated as

$$\frac{dN}{dX} = \frac{c}{H_0} \int_0^\infty n(M, z) \sigma_{\text{DLA}}(M, z) dM, \quad (8)$$

and the column density distribution  $f_{\text{HI}}(N_{\text{HI}}, z)$  is given by

$$f(N_{\text{HI}}, z) \equiv \frac{d^2 n}{dX dN_{\text{HI}}} = \frac{c}{H_0} \int_0^\infty n(M, z) \left| \frac{d\sigma}{dN_{\text{HI}}}(M, z) \right| dM \quad (9)$$

where

$$\frac{d\sigma}{dN_{\text{HI}}} = 2\pi s \frac{ds}{dN_{\text{HI}}}, \quad (10)$$

with  $N_{\text{HI}}(s)$  defined by Equation (6). The density parameter for DLAs,  $\Omega_{\text{DLA}}$  is obtained by integrating the column density distribution

$$\Omega_{\text{DLA}}(N_{\text{HI}}, z) = \frac{m_H H_0}{c \rho_{c,0}} \int_{10^{20.3}}^\infty f_{\text{HI}}(N_{\text{HI}}, z) N_{\text{HI}} dN_{\text{HI}}, \quad (11)$$

where  $\rho_{c,0}$  is the present-day critical density.

At high redshifts, we also use the measurement of  $\Omega_{\text{HI}} b_{\text{HI}}$  from HI intensity mapping at  $z \sim 0.8$  by Switzer et al. (2013). To calculate this quantity in our model, the HI density parameter is given by

$$\Omega_{\text{HI}}(z) = \frac{1}{\rho_{c,0}} \int_0^\infty n(M, z) M_{\text{HI}}(M, z) dM. \quad (12)$$

The bias of HI is given by

$$b_{\text{HI}}(z) = \frac{\int_0^\infty dM n(M, z) b(M, z) M_{\text{HI}}(M, z)}{\int_0^\infty dM n(M, z) M_{\text{HI}}(M, z)} \quad (13)$$

where  $b(M, z)$  is the dark matter halo bias. We fit the HI density profiles of haloes at  $z = 0$  by using the column density distribution at  $z = 0$  for  $N_{\text{HI}} > 10^{20.3} \text{ cm}^{-2}$ , derived from the WHISP data by Zwaan et al. (2005b).

### 3.2 Extending the HIHM relation to high redshifts

We can now extend the HIHM relation developed in Section 2 to higher redshifts. We do this by parameterising the HIHM relation evolution in a manner similar to the parameterisation of the SHM relation evolution by Moster et al. (2013). We write the HIHM relation at higher redshifts as

$$M_{\text{HI}} = 2N_1 M \left[ \left( \frac{M}{M_1} \right)^{-b_1} + \left( \frac{M}{M_1} \right)^{y_1} \right]^{-1}, \quad (14)$$

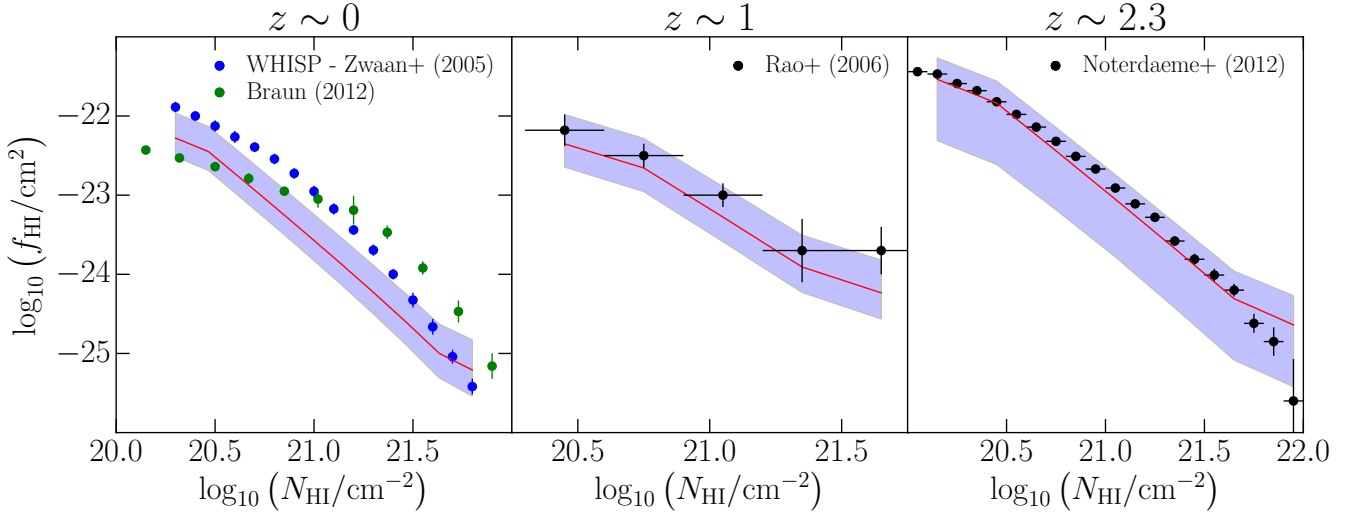


**Figure 6.** The best-fit column density distribution (red curves) in our model at redshifts 0, 1 and 2.3, compared to the observations. The blue shaded regions show the 68% confidence limits. The model fits the high redshift column density distributions quite well but has difficulty in fitting the column density distribution at  $z = 0$ , especially at low column densities.

which has the same form as Equation (2). The parameters in Equation (14) are written as:

$$\begin{aligned} \log_{10} M_1 &= \log_{10} M_{10} + \frac{z}{z+1} M_{11}, \\ N_1 &= N_{10} + \frac{z}{z+1} N_{11}, \\ b_1 &= b_{10} + \frac{z}{z+1} b_{11}, \text{ and} \\ y_1 &= y_{10} + \frac{z}{z+1} y_{11}. \end{aligned} \quad (15)$$

The parameters  $M_{10}$ ,  $N_{10}$ ,  $b_{10}$  and  $y_{10}$  are defined in Equation (2) for  $z = 0$ . The four additional parameters,  $M_{11}$ ,  $N_{11}$ ,  $b_{11}$  and  $y_{11}$ , introduced by Equations (15) govern the evolution of the HIHM at high redshift. These four parameters together with the HI density profile parameter  $c_{\text{HI}}$  are to be constrained from the high redshift observations. This is done by using the data available from  $z = 0$  to 5 as summarised in Table 1. We use the measurements of the incidence rate  $dN/dX$  of DLAs, the column density distribution  $f_{\text{HI}}(N_{\text{HI}}, z)$  of DLAs at high column densities, the three-dimensional clustering of DLAs as quantified by their clustering bias relative to the dark matter, and the total amount of neutral hydrogen in DLAs (Wolfe et al. 1986; Lanzetta et al. 1991; Gardner et al. 1997; Prochaska & Wolfe 2009; Rao et al. 2006; Noterdaeme et al. 2012; Zafar et al. 2013), as well as the measurements of the HI column density distribution and clustering from radio data at  $z < 1$  (Zwaan et al. 2005b; Switzer et al. 2013).

The best-fitting values for the five parameters  $M_{11}$ ,  $N_{11}$ ,  $b_{11}$ ,  $y_{11}$  and  $c_{\text{HI}}$ , and their errors are now estimated by a Bayesian Markov Chain Monte Carlo (MCMC) analysis using the COSMOHAMMER package (Akeret et al. 2013). The likelihood,

$$\mathcal{L} = \exp\left(-\frac{\chi^2}{2}\right) \quad (16)$$

is maximized with respect to the five free parameters, with:

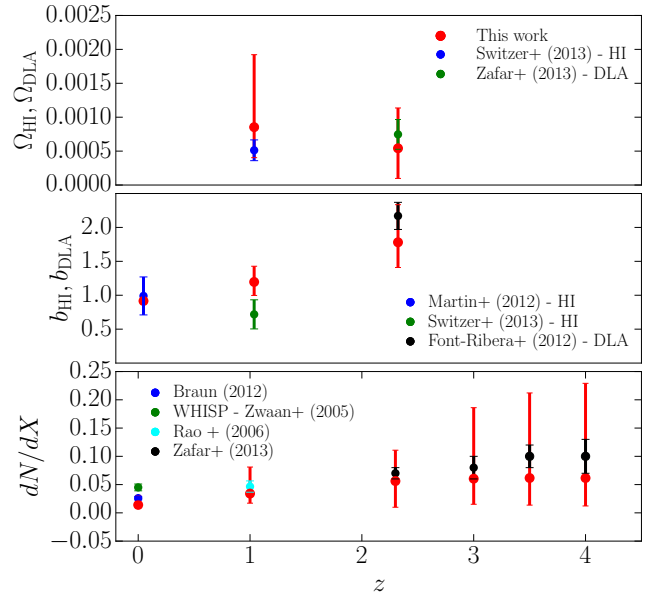


**Figure 7.** Our model predictions for the density parameter, clustering bias, and DLA incidence rate (red, with 68% confidence intervals indicated by the error bars) compared to the observations. Note that at redshift  $z \sim 1$ , Switzer et al. (2013) constrain the product  $\Omega_{\text{HI}} b_{\text{HI}}$ . Shown here is the observed  $\Omega_{\text{HI}} b_{\text{HI}}$  divided by the model value of  $b_{\text{HI}}$  (top panel) and  $\Omega_{\text{HI}}$  (second panel). The model matches these observations, including the bias at high redshifts.

$$\chi^2 = \sum_i \frac{(f_i - f_{\text{obs},i})^2}{\sigma_{\text{obs},i}^2} \quad (17)$$

where the  $f_i$  are the model predictions,  $f_{\text{obs},i}$  are the observational data and  $\sigma_{\text{obs},i}^2$  are the squares of the associated uncertainties (here assumed independent).

The best fitting parameters and their 68% errors are  $\log_{10}(M_{11}/M_{\odot}) = 1.56^{+0.53}_{-2.70}$ ,  $N_{11} = 0.009^{+0.06}_{-0.001}$ ,  $b_{11} = -1.08^{+1.52}_{-0.08}$ ,  $y_{11} = 4.07^{+0.39}_{-2.49}$ , and  $c_{\text{HI}} = 133.66^{+81.39}_{-56.23}$ . The inferred evolution of the four parameters of the HIHM relation in Equation (14) is shown in Figure 5 together with the 68% errors. For comparison, the evolution of the corresponding parameters in the SHM relation parametrization of (Moster et al. 2013) are also shown. The model allows for a wide range of parameters in the HIHM relation at high redshifts. The increase in the best-fitting characteristic mass follows the increase in the characteristic halo mass of the SHM relation. The evolution of the high mass slope  $y_1$  is much more rapid for the HIHM relation than the SHM relation. As we will see below, the high value of the clustering bias factor for DLAs at high redshifts forces the increase in the characteristic halo mass of the HIHM relation but the more gradual increase observed in the DLA incidence rate prevents us from putting too much HI in high mass halos, which constrains the high mass slope to very steep values.

Figure 6 shows the column density distribution derived from our model at  $z \sim 0, 1$ , and  $2.3$  together with the associated 68% statistical error.

At  $z \sim 0$ , only the concentration parameter of the profile is used to obtain the column density distribution, since the HIHM relation has been directly fixed by the results of abundance matching. The concentration parameter is assumed to be equal to that obtained from the fitting of higher redshifts, which is done using the analysis outlined in Sec. 3.2. The relation fits the available data reasonably well, but leads to an underprediction of the observed column density distribution at  $z \sim 0$  at low column densities ( $N_{\text{HI}} < 10^{21.4} \text{ cm}^{-2}$ ).<sup>3</sup> Figure 7 compares other quantities in our model to their observed values. The incidence rate of DLAs is fit very well by the model throughout the redshift range considered here. The measurements of the density parameters of HI and DLAs, and the clustering bias of  $z \sim 2.3$  DLAs are also fit well. The fit to the measured HI bias at  $z = 0$  is also good, although it is somewhat poor at  $z = 1$ .

### 3.3 Comparison to other models of HI at high redshift

Figure 8 shows the inferred best-fitting HIHM at  $z = 0, 1, 2, 3$  and  $4$  in the present model, together with their associated uncertainties. In each case, the black curve shows the best-fit HIHM relation and the grey band shows the 68% scatter around it. The figure also presents a comparison of the HIHM obtained from hydrodynamical simulations and

<sup>3</sup> The two datasets for the column density distribution at  $z \sim 0$  (which indicate a systematic offset) are shown only for comparison, and not directly fitted. The parameters involved in the HIHM are obtained from the abundance matching fits, and the concentration parameter is obtained from the results of the higher-redshift column density fitting. The steep slope of the HIHM relation for  $z = 0$  leads to a lower column density distribution than observed, suggesting that the altered NFW profile may not fully describe the HI density profiles of halos at  $z = 0$ , or that there may be a possible tension between the HI mass function and the column density distribution at  $z = 0$ . We explore this issue in further detail in future work.

other approaches in the literature at  $z = 0, 1, 2$  and  $3$ . These are briefly described below:

(i) At  $z = 0$ , the model that comes closest to the present work is the non-parametric HIHM relation of Marín et al. (2010), although their low-mass slope is shallower.

(ii) The hydrodynamical simulations of Davé et al. (2013) produce an HIHM relation that has very similar high-mass and low-mass slopes as the present HIHM relation. The high characteristic mass of the average best-fitting HIHM relation in the present work is a natural consequence of matching the abundance of haloes with HI-selected galaxies, under the assumption that HI-mass of dark matter haloes scales monotonically with their virial mass.

(iii) Bagla et al. (2010) used a set of analytical prescriptions to populate HI in dark matter haloes. In their simplest model, HI was assigned to dark matter haloes with a constant fraction  $f$  by mass, within a mass range. The maximum and minimum masses of haloes that host HI were assumed to be redshift-dependent. It was also assumed that haloes with virial velocities of greater than 200 km/s and less than 30 km/s do not host any HI.

(iv) Gong et al. (2011) provide nonlinear analytical forms of the HIHM relation at  $z = 1, 2$  and  $3$ , derived from the results of the simulations of Obreschkow et al. (2009). These predict a slightly different form for the HIHM relation.

(v) The model of Barnes & Haehnelt (2014) uses an HIHM relation that reproduces the observed bias of DLA systems at  $z \sim 2.3$ , and constrains stellar feedback in shallow potential wells.

(vi) Padmanabhan & Refregier (2016) used a statistical data-driven approach to derive the best-fitting HIHM relation and radial distribution profile  $\rho_{\text{HI}}(r)$  for  $z = 0-4$ , from a joint analysis combining the data from the radio observations at low redshifts and the Damped Lyman-Alpha (DLA) system observables at high redshifts, along the lines of the present work. This approach also produces results consistent with the present work, although the present best-fit HIHM relation at high redshifts may prefer a higher characteristic halo mass.

It can be seen that all these models are consistent with each other and with the data at the 68% confidence level. Tighter constraints on the HIHM relation at high redshifts may be achieved with the availability of better quality data with upcoming radio telescopes.

## 4 CONCLUSIONS

In this paper, we have explored the evolution of the neutral hydrogen content of galaxies in the last 12 Gyr (redshifts  $z = 0-4$ ). At redshift  $z = 0$ , this work follows the approach of abundance matching, which has been widely used for the stellar mass content of galaxies to model galaxy luminosity functions (Vale & Ostriker 2004, 2006; Conroy et al. 2006; Shankar et al. 2006b; Guo et al. 2010; Behroozi et al. 2010; Moster et al. 2010, 2013). A parameterised functional form for a monotonic relationship between the HI and halo mass is assumed to obtain the HI- Halo Mass (HIHM) relation. The best fit values of the parameters that fit the observed HI mass function from radio data are then obtained. This approach of modelling the HIHM relation at  $z = 0$  from the

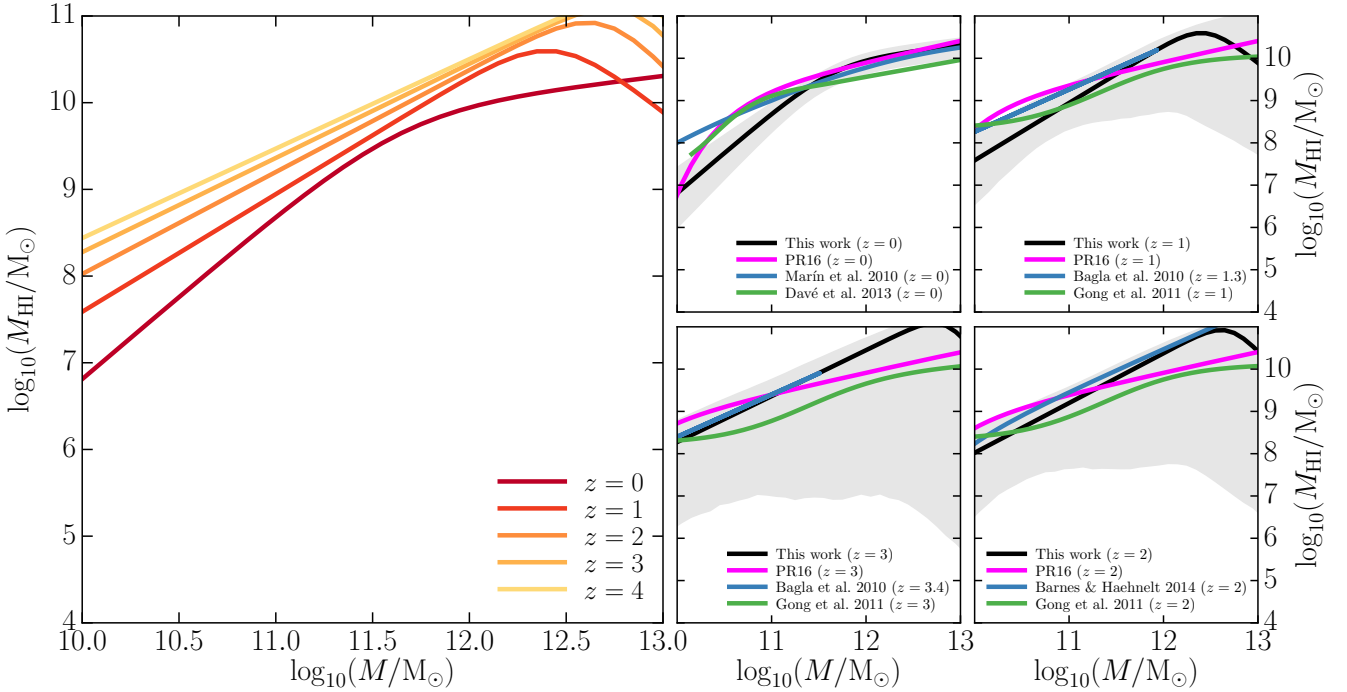


**Figure 8.** *Left panel:* The HIHM relation inferred at redshifts  $z = 0, 1, 2, 3$  and  $4$  from the present work. *Right panels:* The HIHM relation relation in the present work compared to the results of other approaches in the literature at redshifts  $z = 0, 1, 2$  and  $3$ .

radio data at low redshifts has been followed previously by Papastergis et al. (2013). Our abundance matched HIHM agrees with that derived by these authors.

We further explore how well the abundance matching approach at  $z = 0$  can be constrained by fitting to the high redshift data. We extend the low redshift determination of the HIHM relation by postulating that the evolution of the HIHM relation is similar to the stellar-to-halo-mass (SHM) relation. We parameterize this evolution analogously to the evolution of the SHM relation by Moster et al. (2013). The physical motivation for the parametrization is that the HI-follows-stars functional form works well at low redshifts, which is in turn a consequence of the fact that the underlying mass/luminosity functions can both be described by the Schechter form. Observational measurements of the HI mass function are not yet available at these redshifts. Hence, we use measurements of the HI column density distribution function and the HI clustering from UV/optical observations of quasar absorption spectra. We assume that high column density systems (DLAs;  $N_{\text{HI}} > 10^{20.3} \text{ cm}^{-2}$ ) probe systems are high-redshift analogs of HI in galaxies detected in radio surveys at low redshifts (Zwaan et al. 2005b).

Our procedure allows a modeling of low and high redshift measurements of the HI content of galaxies to obtain the evolution of the HIHM relation from  $z = 0$  to  $2.3$  with the associated uncertainty. This technique is complementary to the forward modelling approach which aims to characterize HI using a halo model framework similar to that of the underlying dark matter (Padmanabhan & Refregier 2016). However, the present work represents a first attempt to characterize the HIHM relation empirically, directly from the data. Due to the sparse nature of the high-redshift data

at present, there is considerable scatter in the high-redshift HIHM relation. As a result, other apparently dissimilar models from the literature are also consistent with the data and the allowed range of the present work. The scatter in the HIHM relation at higher redshifts can be reduced with tighter constraints on the HI mass functions from upcoming and future radio surveys.

Our results provide a useful benchmark to calibrate the HI physics in hydrodynamical simulations, especially at low redshifts where correct treatment of star formation and feedback as well as cooling and formation of molecular hydrogen are critical. They also provide an estimate of the uncertainty in the HIHM relation coming from the high-redshift data, and motivate further work towards possibly tighter constraints on the HIHM relation.

## ACKNOWLEDGEMENTS

We thank Alireza Rahmati, Alexandre Refregier and Sergey Koposov for useful discussions, and Robert Crain for kindly providing the data from the EAGLE simulations. This work has made use of the VizieR catalogue access tool, CDS, Strasbourg, France. The original description of the VizieR service was published in the A&AS 143, 23. HP’s research is supported by the Tomalla Foundation. GK gratefully acknowledges support from the ERC Advanced Grant 320596 ‘The Emergence of Structure During the Epoch of Reionization’.

## REFERENCES

- Abazajian K. N., et al., 2009, *ApJS*, **182**, 543
- Akeret J., Seehars S., Amara A., Refregier A., Csillaghy A., 2013, *Astronomy and Computing*, **2**, 27
- Bagla J. S., Khandai N., Datta K. K., 2010, *MNRAS*, **407**, 567
- Bahé Y. M., et al., 2016, *MNRAS*, **456**, 1115
- Baldry I. K., Glazebrook K., Driver S. P., 2008, *MNRAS*, **388**, 945
- Bandura K., et al., 2014, in *Ground-based and Airborne Telescopes V*. p. 914522 ([arXiv:1406.2288](#)), doi:10.1117/12.2054950
- Barkana R., 2016, preprint, ([arXiv:1605.04357](#))
- Barnes L. A., Haehnelt M. G., 2009, *MNRAS*, **397**, 511
- Barnes L. A., Haehnelt M. G., 2010, *MNRAS*, **403**, 870
- Barnes L. A., Haehnelt M. G., 2014, *MNRAS*, **440**, 2313
- Behroozi P. S., Conroy C., Wechsler R. H., 2010, *ApJ*, **717**, 379
- Berry M., Somerville R. S., Haas M. R., Gawiser E., Maller A., Popping G., Trager S. C., 2014, *MNRAS*, **441**, 939
- Bird S., Vogelsberger M., Haehnelt M., Sijacki D., Genel S., Torrey P., Springel V., Hernquist L., 2014, *MNRAS*, **445**, 2313
- Bird S., Haehnelt M., Neeleman M., Genel S., Vogelsberger M., Hernquist L., 2015, *MNRAS*, **447**, 1834
- Blanton M. R., Moustakas J., 2009, *ARA&A*, **47**, 159
- Bouché N., et al., 2010, *ApJ*, **718**, 1001
- Boylan-Kolchin M., Springel V., White S. D. M., Jenkins A., Lemson G., 2009, *MNRAS*, **398**, 1150
- Catinella B., et al., 2010, *MNRAS*, **403**, 683
- Catinella B., et al., 2012, *A&A*, **544**, A65
- Catinella B., et al., 2013, *MNRAS*, **436**, 34
- Cen R., 2012, *ApJ*, **748**, 121
- Chang T.-C., Pen U.-L., Bandura K., Peterson J. B., 2010, *Nature*, **466**, 463
- Conroy C., Wechsler R. H., Kravtsov A. V., 2006, *ApJ*, **647**, 201
- Crain R. A., et al., 2015, *MNRAS*, **450**, 1937
- Crain R. A., et al., 2016, preprint, ([arXiv:1604.06803](#))
- Davé R., Katz N., Oppenheimer B. D., Kollmeier J. A., Weinberg D. H., 2013, *MNRAS*, **434**, 2645
- Delhaize J., Meyer M. J., Staveley-Smith L., Boyle B. J., 2013, *MNRAS*, **433**, 1398
- Duffy A. R., Kay S. T., Battye R. A., Booth C. M., Dalla Vecchia C., Schaye J., 2012, *MNRAS*, **420**, 2799
- Evoli C., Salucci P., Lapi A., Danese L., 2011, *ApJ*, **743**, 45
- Fabello S., Kauffmann G., Catinella B., Li C., Giovanelli R., Haynes M. P., 2012, *MNRAS*, **427**, 2841
- Font-Ribera A., et al., 2012, *J. Cosmology Astropart. Phys.*, **11**, 59
- Fu J., Guo Q., Kauffmann G., Krumholz M. R., 2010, *MNRAS*, **409**, 515
- Fu J., Kauffmann G., Li C., Guo Q., 2012, *MNRAS*, **424**, 2701
- Gardner J. P., Katz N., Hernquist L., Weinberg D. H., 1997, *ApJ*, **484**, 31
- Giovanelli R., et al., 2005, *AJ*, **130**, 2598
- Gong Y., Chen X., Silva M., Cooray A., Santos M. G., 2011, *ApJ*, **740**, L20
- Guha Sarkar T., Mitra S., Majumdar S., Choudhury T. R., 2012, *MNRAS*, **421**, 3570
- Guo Q., White S., Li C., Boylan-Kolchin M., 2010, *MNRAS*, **404**, 1111
- Haehnelt M. G., Rauch M., Steinmetz M., 1996, *MNRAS*, **283**, 1055
- Haehnelt M. G., Steinmetz M., Rauch M., 1998, *ApJ*, **495**, 647
- Hong S., Katz N., Davé R., Fardal M., Kereš D., Oppenheimer B. D., 2010, [arXiv:1008.4242](#),
- Jonas J. L., 2009, *IEEE Proceedings*, **97**, 1522
- Kauffmann G., Huang M.-L., Moran S., Heckman T. M., 2015, *MNRAS*, **451**, 878
- Kim H.-S., Power C., Baugh C. M., Wyithe J. S. B., Lacey C. G., Lagos C. D. P., Frenk C. S., 2013, *MNRAS*, **428**, 3366
- Kim H.-S., Wyithe J. S. B., Baugh C. M., Lagos C. d. P., Power C., Park J., 2016, preprint, ([arXiv:1603.02383](#))
- Krumholz M. R., Dekel A., 2012, *ApJ*, **753**, 16
- Kulkarni G., Rollinde E., Hennawi J. F., Vangioni E., 2013, *ApJ*, **772**, 93
- Lagos C. D. P., Baugh C. M., Lacey C. G., Benson A. J., Kim H.-S., Power C., 2011, *MNRAS*, **418**, 1649
- Lagos C. d. P., Davis T. A., Lacey C. G., Zwaan M. A., Baugh C. M., Gonzalez-Perez V., Padilla N. D., 2014, *MNRAS*, **443**, 1002
- Lah P., et al., 2007, *MNRAS*, **376**, 1357
- Lah P., et al., 2009, *MNRAS*, **399**, 1447
- Lanzetta K. M., Wolfe A. M., Turnshek D. A., Lu L., McMahon R. G., Hazard C., 1991, *ApJS*, **77**, 1
- Leroy A. K., Walter F., Brinks E., Bigiel F., de Blok W. J. G., Madore B., Thornley M. D., 2008, *AJ*, **136**, 2782
- Leroy A. K., et al., 2009, *AJ*, **137**, 4670
- Li C., White S. D. M., 2009, *MNRAS*, **398**, 2177
- Li C., Kauffmann G., Fu J., Wang J., Catinella B., Fabello S., Schiminovich D., Zhang W., 2012, *MNRAS*, **424**, 1471
- Macciò A. V., Dutton A. A., van den Bosch F. C., Moore B., Potter D., Stadel J., 2007, *MNRAS*, **378**, 55
- Maller A. H., Bullock J. S., 2004, *MNRAS*, **355**, 694
- Maller A. H., Prochaska J. X., Somerville R. S., Primack J. R., 2001, *MNRAS*, **326**, 1475
- Marín F. A., Gnedin N. Y., Seo H.-J., Vallinotto A., 2010, *ApJ*, **718**, 972
- Martin A. M., Papastergis E., Giovanelli R., Haynes M. P., Springob C. M., Stierwalt S., 2010, *ApJ*, **723**, 1359
- Martindale H., Thomas P. A., Henriques B. M., Loveday J., 2016, preprint, ([arXiv:1606.08440](#))
- Masui K. W., et al., 2013, *ApJ*, **763**, L20
- Meyer M. J., et al., 2004, *MNRAS*, **350**, 1195
- Moster B. P., Somerville R. S., Maulbetsch C., van den Bosch F. C., Macciò A. V., Naab T., Oser L., 2010, *ApJ*, **710**, 903
- Moster B. P., Naab T., White S. D. M., 2013, *MNRAS*, **428**, 3121
- Nagamine K., Wolfe A. M., Hernquist L., Springel V., 2007, *ApJ*, **660**, 945
- Navarro J. F., Frenk C. S., White S. D. M., 1996, *ApJ*, **462**, 563
- Noterdaeme P., et al., 2012, *A&A*, **547**, L1
- Obreschkow D., Croton D., De Lucia G., Khochfar S., Rawlings S., 2009, *ApJ*, **698**, 1467
- Padmanabhan H., Refregier A., 2016, preprint, ([arXiv:1607.01021](#))
- Padmanabhan H., Choudhury T. R., Refregier A., 2015, *MNRAS*, **447**, 3745
- Padmanabhan H., Choudhury T. R., Refregier A., 2016, *MNRAS*, **458**, 781
- Papastergis E., Cattaneo A., Huang S., Giovanelli R., Haynes M. P., 2012, *ApJ*, **759**, 138
- Papastergis E., Giovanelli R., Haynes M. P., Rodríguez-Puebla A., Jones M. G., 2013, *ApJ*, **776**, 43
- Pérez-González P. G., et al., 2008, *ApJ*, **675**, 234
- Pontzen A., et al., 2008, *MNRAS*, **390**, 1349
- Popping A., Davé R., Braun R., Oppenheimer B. D., 2009, *A&A*, **504**, 15
- Popping G., Somerville R. S., Trager S. C., 2014, *MNRAS*, **442**, 2398
- Popping G., Behroozi P. S., Peebles M. S., 2015, *MNRAS*, **449**, 477
- Prochaska J. X., Wolfe A. M., 1997, *ApJ*, **487**, 73
- Prochaska J. X., Wolfe A. M., 2009, *ApJ*, **696**, 1543
- Rahmati A., Schaye J., 2014, *MNRAS*, **438**, 529
- Rahmati A., Pawlik A. H., Raicevic M., Schaye J., 2013, *MNRAS*, **430**, 2427
- Rao S., Briggs F., 1993, *ApJ*, **419**, 515

- Rao S. M., Turnshek D. A., Nestor D. B., 2006, *ApJ*, **636**, 610
- Rhee J., Zwaan M. A., Briggs F. H., Chengalur J. N., Lah P., Oosterloo T., Hulst T. v. d., 2013, *MNRAS*, **435**, 2693
- Rodríguez-Puebla A., Avila-Reese V., Firmani C., Colín P., 2011, *Rev. Mex. Astron. Astrofis.*, **47**, 235
- Saintonge A., et al., 2011a, *MNRAS*, **415**, 32
- Saintonge A., et al., 2011b, *MNRAS*, **415**, 61
- Santini P., et al., 2012, *A&A*, **538**, A33
- Santos M., et al., 2015, *Advancing Astrophysics with the Square Kilometre Array (AASKA14)*, p. 19
- Sarkar D., Bharadwaj S., Anathpindika S., 2016, preprint, ([arXiv:1605.02963](https://arxiv.org/abs/1605.02963))
- Schaye J., et al., 2015, *MNRAS*, **446**, 521
- Scoccamarro R., Sheth R. K., Hui L., Jain B., 2001, *ApJ*, **546**, 20
- Shankar F., Lapi A., Salucci P., De Zotti G., Danese L., 2006a, *ApJ*, **643**, 14
- Shankar F., Lapi A., Salucci P., De Zotti G., Danese L., 2006b, *ApJ*, **643**, 14
- Sheth R. K., Tormen G., 2002, *MNRAS*, **329**, 61
- Somerville R. S., Davé R., 2015, *ARA&A*, **53**, 51
- Somerville R. S., Popping G., Trager S. C., 2015, *MNRAS*, **453**, 4337
- Springel V., et al., 2005, *Nature*, **435**, 629
- Switzer E. R., et al., 2013, *MNRAS*, **434**, L46
- Tescari E., Viel M., Tornatore L., Borgani S., 2009, *MNRAS*, **397**, 411
- Vale A., Ostriker J. P., 2004, *MNRAS*, **353**, 189
- Vale A., Ostriker J. P., 2006, *MNRAS*, **371**, 1173
- Walter F., Brinks E., de Blok W. J. G., Bigiel F., Kennicutt Jr. R. C., Thornley M. D., Leroy A., 2008, *AJ*, **136**, 2563
- Wolfe A. M., Turnshek D. A., Smith H. E., Cohen R. D., 1986, *ApJS*, **61**, 249
- Wyithe J. S. B., Brown M. J. I., 2010, *MNRAS*, **404**, 876
- York D. G., et al., 2000, *AJ*, **120**, 1579
- Zafar T., Péroux C., Popping A., Milliard B., Deharveng J.-M., Frank S., 2013, *A&A*, **556**, A141
- Zhang W., Li C., Kauffmann G., Xiao T., 2013, *MNRAS*, **429**, 2191
- Zwaan M. A., Meyer M. J., Staveley-Smith L., Webster R. L., 2005a, *MNRAS*, **359**, L30
- Zwaan M. A., van der Hulst J. M., Briggs F. H., Verheijen M. A. W., Ryan-Weber E. V., 2005b, *MNRAS*, **364**, 1467
- van de Voort F., Schaye J., Booth C. M., Haas M. R., Dalla Vecchia C., 2011, *MNRAS*, **414**, 2458
- van der Hulst J. M., van Albada T. S., Sancisi R., 2001, in Hibbard J. E., Rupen M., van Gorkom J. H., eds, *Astronomical Society of the Pacific Conference Series Vol. 240, Gas and Galaxy Evolution*. p. 451

This paper has been typeset from a  $\text{\TeX}/\text{\LaTeX}$  file prepared by the author.